Article:
Li, Y. (2011) Small-scale intermittency and local anisotropy in turbulent mixing with rotation. Journal of Turbulence, 12 (38). pp. 1-21. ISSN: 1468-5248

https://doi.org/10.1080/14685248.2011.613398

Journal of Turbulence
Vol. 00, No. 00, 2011, 1–22

RESEARCH ARTICLE

Small-scale intermittency and local anisotropy in turbulent mixing with rotation

Yi Li*
School of Mathematics and Statistics, University of Sheffield, Sheffield, S3 7RH, UK
(*Received 00 Month 200x; final version received 00 Month 200x*)

The statistics of the velocity gradient and the gradient of a passive scalar in rotating turbulence are studied using Lagrangian stochastic models. Models for the velocity gradients are derived generalizing the approach proposed in Chevillard and Meneveau [Phys. Rev. Lett. **97**, 174501(200)], whereas the scalar gradients are described using the model proposed by Gonzalez in Phys. Fluids **21**, 055104 (2009). The non-Gaussian and anisotropic statistics of the gradients are analyzed, and compared with available results in the literature. It is found that the models reproduce the observation that rotation tends to reduce small-scale intermittency for both velocity and scalar gradients. The models predict the skewness of transverse velocity gradient components in the perpendicular plane and its non-monotonic dependence on the rotation rate. The models also reproduce the anisotropy in the scalar gradient at intermediate Rossby numbers. Furthermore, we show that the anisotropy is reached at an intermediate rotation rate, and the maximum coincides with a transition in the relative importance of the self and cross production terms for the scalar gradient.

Keywords: Homogeneous rotating turbulence; Lagrangian stochastic models; turbulent mixing; small-scale intermittency; local anisotropy

1. Introduction

Rotating turbulence is routinely observed in industrial, geophysical and astrophysical flows. Rotation has tremendous effects on the small-scale statistics in turbulence, in particular those of the velocity and scalar gradients. In non-rotating turbulence, the probability density functions (PDF) of the velocity and scalar gradients are highly non-Gaussian due to small scale intermittency. Typically, the tails of the PDFs can be fitted by an exponential or a stretched exponential [1, 2]. The modelling of the non-Gaussian statistics of the small-scale statistics is a main unsolved problem in the theory and simulation of turbulent flows. In rotating turbulence, the statistics of velocity gradient are reported in, e.g., [3–5]. It is observed that strong fluctuations in the gradients are suppressed by rotation, so that the deviation from Gaussian distribution is reduced. It is found [4, 6] that the skewness of the longitudinal velocity gradient decreases with the Rossby number. Furthermore, rotation also induces anisotropy in small scale statistics. The cyclonic vorticity component develops a positive skewness in rotating turbulence. The skewness is the strongest at intermediate rotation rates [4, 5, 7, 8]. In a DNS study of the mixing of passive scalars in rotating turbulence, [9] reports that the small-scale intermittency in the gradients of the passive scalar is also reduced. The flatness decreases with increasing rotation rates. Meanwhile, the scalar gradients also become anisotropic. The root-mean-square (RMS) value of the component along the rotation axis decays

*Email: yili@shef.ac.uk

ISSN: 1468-5248 (online only)

DOI: 10.1080/14685240YYxxxxxxx
http://www.informaworld.com

faster than the perpendicular components. The flatness of the parallel component is smaller than that of the perpendicular components. The authors explain the anisotropy by the reduced spectral transfer for the parallel component and large scale anisotropy in the velocity field.

While much has been learned about the velocity and scalar gradients in rotating turbulence, several questions remain unanswered. In particular, how does the anisotropy in the scalar gradient depend on rotation rates? If any nontrivial relation exists, what are the mechanisms? In this paper, we attempt to gain some understanding of these questions via a modelling study, using Lagrangian stochastic models for the velocity and scalar gradients.

Lagrangian stochastic models for the velocity and scalar gradients have been used extensively to study and model small scale intermittency, contaminant dispersion, turbulent combustion and many other phenomena [10–19]. Thus, generalization of the models to include the effects of rotation will be useful for many applications as well. On the other hand, although we should keep the modelling assumptions in mind when we interpret the results, stochastic models have provided useful insights into the physics of turbulence. With the simplicity of the models, these usually can be obtained with significantly less computational costs. Therefore, the purpose of this paper is two fold. First, we intend to propose a stochastic model for the velocity gradient in rotating turbulence. Second, we examine the prediction of the model, and use the model to study some aspects of the mixing as well as the dynamics of the small scales of rotating turbulence. We first generalize the Lagrangian stochastic model proposed in [15, 20] to rotating turbulence. The model makes use of the recent deformation of a fluid element along its path to model the unclosed terms [15, 20]. In our generalization, both the direct effects of rotation and the effects on the recent deformation history of the fluid element are considered. Model predictions are checked against some of the results reported in the literature. We then use the model, together with the model for the gradient of a passive scalar proposed in [19], to study the dynamics of the velocity gradient and the passive scalar gradient in rotating turbulence. We focus primarily on the non-Gaussian statistics and the anisotropy of the gradients, and the dependence on rotation rates.

The paper is organized as follows. The background and the derivation of the models are introduced in the next section. The numerical solution method and results are discussed in Section 3. The paper is concluded in Section 4.

2. Stochastic models for the velocity and passive scalar gradients

2.1. *Background*

We consider incompressible flows in a frame of reference rotating with a constant angular velocity $\mathbf{\Omega} = \Omega\mathbf{k}$. The velocity field $\mathbf{u}(\mathbf{x}, t)$ is governed by

$$\frac{d\mathbf{u}}{dt} \equiv \partial_t \mathbf{u} + (\mathbf{u}\cdot\nabla)\mathbf{u} = -2\mathbf{\Omega}\times\mathbf{u} - \nabla p + \nu\nabla^2\mathbf{u}\ , \tag{1}$$

where $d/dt \equiv \partial_t + \mathbf{u}\cdot\nabla$ denotes the material derivative, p is the pressure divided by the constant density of the fluid, and ν the kinematic viscosity. The equation for the velocity gradient tensor $\mathbf{A}$, defined as $A_{ij} = \partial u_i/\partial x_j = \partial_j u_i$, is obtained by taking the gradient of the above equation. The equation reads

$$\frac{d\mathbf{A}}{dt} = -\mathbf{A}^2 - 2\mathbf{\Omega}\times\mathbf{A} - \nabla\nabla p + \nu\nabla^2\mathbf{A}, \tag{2}$$

where the tensor $\mathbf{\Omega}\times\mathbf{A}$ is defined by $(\mathbf{\Omega}\times\mathbf{A})_{ij}=\epsilon_{imn}\Omega_m A_{nj}$. $\nabla\nabla p$ is the pressure Hessian tensor with components $\partial^2_{ij}p$. For incompressible flows, the divergence of the velocity field is zero, i.e., $\mathrm{Tr}\mathbf{A}=0$. Taking the trace of the above equation, one finds the Poisson equation for the pressure

$$\nabla^2 p=-\mathrm{Tr}\mathbf{A}^2+2\mathbf{\Omega}\cdot\boldsymbol{\omega}, \tag{3}$$

where $\boldsymbol{\omega}=\nabla\times\mathbf{u}$ is the vorticity vector. A number of physical processes contribute to the evolution of the velocity gradient. The first two terms on the right hand side of Eq. (2) represent the self-stretching and the Coriolis effects, respectively. The last two terms are contributions from the pressure Hessian and the viscous diffusion. In a Lagrangian stochastic model, the available information is the time series of the velocity gradient on a fluid particle. Therefore, the last two terms in Eq. (2) are not closed. The main task is to model the two terms using the time history of the velocity gradient, so that realistic statistics for the gradient are reproduced.

Let $\phi(\mathbf{x},t)$ denote a passive scalar field. The equation for ϕ is

$$\frac{d\phi}{dt}=\Gamma\nabla^2\phi \tag{4}$$

where Γ is the molecular diffusivity of the scalar. We consider the gradient of the passive scalar, denoted by $\mathbf{G}$ with components $G_i=\partial_i\phi$. The evolution of $\mathbf{G}$ is given by

$$\frac{d\mathbf{G}}{dt}=-\mathbf{A}^T\mathbf{G}+\Gamma\nabla^2\mathbf{G}, \tag{5}$$

which is obtained by taking the gradient of Eq. (4). The first term on the right hand side (RHS) is the production term of $\mathbf{G}$, which shows that $\mathbf{G}$ is generated when the velocity gradient squeezes different patches of scalar together. The second term is the molecular diffusion term. In a stochastic model that couples the evolution of $\mathbf{A}$ and $\mathbf{G}$, the production term is closed, but the diffusion term in Eq. (5) need to be modelled.

For non-rotating turbulence, the equation for $\mathbf{A}$ and the pressure Poisson equation are obtained from Eq. (2) and Eq. (3), respectively, by setting $\mathbf{\Omega}=0$. As mentioned before, several models for the velocity gradient in non-rotating turbulence have been proposed [11–15]. Among these models, the model in [11] leads to stationary statistics, as required in stationary turbulence. It is however assumed that $\mathrm{Tr}(\mathbf{A}\mathbf{A}^T)$ (the so-called pseudo-dissipation) follows the log-normal distribution, which is no longer true in rotating turbulence. On the other hand, the model in [15] also produces stationary statistics and is shown to reproduce rather well the statistics of velocity gradient in a range of tests [15, 20, 21]. Meanwhile, the model does not rely on specific assumptions that are known to be invalid in rotating turbulence. Therefore, we use the model proposed in [15] as a starting point, and now generalize it (called CM model hereafter) to include the effects of rotation.

2.2. *Stochastic model for velocity gradient*

In a Lagrangian stochastic model for the velocity gradient, the time history of the velocity gradient is available. Let $\mathcal{A}\equiv\{\mathbf{A}(s):s\le t\}$ denote the time history up to time t. Ideally, the model should reproduce the multi-time joint PDF of the gradient. As is noted in, e.g., [22, 23], this can be achieved as long as one has a precise model for the conditional rate of change for $\mathbf{A}(t)$, $\langle d\mathbf{A}(t)/dt|\mathcal{A}\rangle$, where $\langle\cdots\rangle$

denotes ensemble average. According to (2), the conditional rate of change is given by

$$\left\langle \frac{d\mathbf{A}}{dt} \middle| \mathcal{A} \right\rangle = -\mathbf{A}^2 - 2\boldsymbol{\Omega} \times \mathbf{A} - \langle \nabla\nabla p | \mathcal{A} \rangle + \langle \nu \nabla^2 \mathbf{A} | \mathcal{A} \rangle. \tag{6}$$

The self-stretching term and the Coriolis force on the RHS are closed, since they depend deterministically on the velocity gradient. We need to model the conditional averages $\langle \nabla\nabla p|\mathcal{A}\rangle$ and $\langle \nu\nabla^2\mathbf{A}|\mathcal{A}\rangle$.

Note that $\langle \partial^2_{ij} p|\mathcal{A}\rangle$ is the average conditioned on the entire time series. However, due to Lagrangian decorrelation, one expects that the information for the velocity gradient at early time is not important in the conditional average. The DNS analysis in [24] indeed confirms the tendency of Lagrangian decorrelation. For filtered DNS data, the analysis shows that the decorrelation occurs at few eddy turnover time at the cutoff scale. Using τ to denote the decorrelation time scale for the velocity gradient, the above argument thus implies that

$$\langle \partial^2_{ij} p|\mathcal{A}\rangle \approx \langle \partial^2_{ij} p|\mathcal{A}_\tau\rangle, \tag{7}$$

where $\mathcal{A}_\tau \equiv \{\mathbf{A}(s) : t-\tau \le s \le t\}$ denotes the recent time history of $\mathbf{A}$ from time $t-\tau$ to t. Similarly, we can write

$$\langle \nu\nabla^2\mathbf{A}|\mathcal{A}\rangle \approx \langle \nu\nabla^2\mathbf{A}|\mathcal{A}_\tau\rangle. \tag{8}$$

and as a consequence the evolution of $\mathbf{A}(t)$ can be modelled by the following equation:

$$\frac{d\mathbf{A}}{dt} = -\mathbf{A}^2 - 2\boldsymbol{\Omega}\times\mathbf{A} - \langle \nabla\nabla p|\mathcal{A}_\tau\rangle + \langle \nu\nabla^2\mathbf{A}|\mathcal{A}_\tau\rangle. \tag{9}$$

The system is to be closed by the models for the conditional averages. Note that Eqs. (7) and (8) are essentially the "recent fluid deformation" approximation made in [15] (see also [24]), rephrased in terms of the conditional averages.

We first consider the conditional average of the pressure Hessian. As is presented in the CM model, the idea is to make use of the deformation history of fluid elements during their Lagrangian evolution. Let $\mathbf{X}$ denote the location of a fluid particle at time $t-\tau$, and $\mathbf{x}(t)$ denote the location of the same particle at time t. $\mathbf{X}$ can be taken as the Lagrangian coordinates of the fluid particle. The deformation and rotation of a fluid element is described by the deformation gradient $\mathbf{D}$ where $D_{ij} \equiv \partial x_i/\partial X_j$. $\mathbf{D}$ evolves according to $d\mathbf{D}/dt = \mathbf{A}\mathbf{D}$, therefore is determined by the time history $\mathcal{A}_\tau$. The solution can be written in terms of the "time-ordered matrix exponential ":

$$\mathbf{D}(t) = \mathcal{T}\exp^+\left[\int_{t-\tau}^{t} \mathbf{A}(s)ds\right], \tag{10}$$

where $\mathcal{T}\exp^+$ is the notation for the time-ordered matrix exponential. We will in the following also use the Cauchy-Green tensor $\mathbf{C} \equiv \mathbf{D}\mathbf{D}^T$, and the inverse of the deformation gradient $\mathbf{D}^{-1}$. The (i,j) element of $\mathbf{D}^{-1}$ is $\partial X_i/\partial x_j$, denoted as D^{-1}_{ij}. Obviously, $\mathbf{C}^{-1} = \mathbf{D}^{-T}\mathbf{D}^{-1}$ and $C^{-1}_{ij} = D^{-1}_{ki}D^{-1}_{kj}$.

Changing the coordinates from $\mathbf{x}(t)$ to $\mathbf{X}$, we have for the conditional pressure Hessian:

$$\langle \partial_{ij}^2 p(t)|\mathcal{A}_\tau\rangle = \left\langle D_{mi}^{-1}D_{nj}^{-1}\frac{\partial^2 p}{\partial X_m \partial X_n}\middle|\mathcal{A}_\tau\right\rangle + \left\langle \frac{\partial D_{mj}^{-1}}{\partial x_i}\frac{\partial p}{\partial X_m}\middle|\mathcal{A}_\tau\right\rangle. \tag{11}$$

The second term on the RHS involves the spatial variation of the deformation gradient. It represents the effects of neighboring fluid particles. As proposed in [15], this term is neglected. Note further that $\mathbf{D}^{-1}$ is a deterministic function of the time history $\mathcal{A}_\tau$, therefore it can be taken out of the average. We thus find

$$\langle \partial_{ij}^2 p|\mathcal{A}_\tau\rangle \approx D_{mi}^{-1}D_{nj}^{-1}\left\langle \frac{\partial^2 p}{\partial X_m \partial X_n}\middle|\mathcal{A}_\tau\right\rangle. \tag{12}$$

$\partial^2 p/\partial X_m \partial X_n$ is called the Lagrangian pressure Hessian. It measures the changes in the pressure of the fluid particle at time t when it is displaced from its initial location slightly at time $t-\tau$. For sufficiently large time delay τ, it is reasonable to assume that the conditional average is isotropic. Hence we may write $\langle \partial^2 p/\partial X_m \partial X_n|\mathcal{A}_\tau\rangle = \delta_{mn}N$, N to be determined, and

$$\langle \partial_{ij}^2 p|\mathcal{A}_\tau\rangle = D_{mi}^{-1}D_{mj}^{-1}N = C_{ij}^{-1}N. \tag{13}$$

N will be chosen to reproduce the correct Laplacian of the pressure. Taking the trace of the above equation, and making use of the pressure Poisson equation [Eq. (3)], we find

$$-\mathrm{Tr}\mathbf{A}^2 + 2\boldsymbol{\Omega}\cdot\boldsymbol{\omega} = N\mathrm{Tr}\mathbf{C}^{-1}, \tag{14}$$

from which N can be found, giving

$$\langle \partial_{ij}^2 p|\mathcal{A}_\tau\rangle = \frac{C_{ij}^{-1}}{\mathrm{Tr}\mathbf{C}^{-1}}(2\boldsymbol{\Omega}\cdot\boldsymbol{\omega} - \mathrm{Tr}\mathbf{A}^2). \tag{15}$$

C_{ij}^{-1} in the above equation is known from the time history of $\mathbf{A}$. Thus, in principle, the above expression already constitutes a closed model. Nevertheless, further simplification is desirable to avoid the calculation of the time-ordered matrix exponential. As in the CM model, we assume $\mathbf{A}(s)$ to be constant over the time interval $[t-\tau, t]$, i.e., $\mathbf{A}(s) \approx \mathbf{A}(t)$ (we will discuss this approximation further below). Hence, $\mathbf{D}(t) \approx \mathbf{D}_\tau(t) \equiv \exp[\tau\mathbf{A}(t)]$, and

$$\mathbf{C}^{-1} \approx \mathbf{C}_\tau^{-1} \equiv e^{-\tau\mathbf{A}^T}e^{-\tau\mathbf{A}}. \tag{16}$$

With $\mathbf{C}^{-1}$ replaced by $\mathbf{C}_\tau^{-1}$, we obtain the final model for the conditional pressure Hessian

$$\langle \nabla\nabla p|\mathcal{A}_\tau\rangle = \frac{\mathbf{C}_\tau^{-1}}{\mathrm{Tr}\mathbf{C}_\tau^{-1}}(2\boldsymbol{\Omega}\cdot\boldsymbol{\omega} - \mathrm{Tr}\mathbf{A}^2). \tag{17}$$

Compared with the CM model, system rotation introduces the new term $2\boldsymbol{\Omega}\cdot$

$\boldsymbol{\omega}$. Obviously, the Cauchy-Green tensor $\mathbf{C}_\tau$ is also affected indirectly, since the statistics of the velocity gradient are modified by rotation.

For the conditionally averaged viscous diffusion term $\langle \nu \nabla^2 \mathbf{A} | \mathcal{A}_\tau \rangle$, we too apply the Lagrangian-Eulerian coordinate substitution. Omitting again the contribution from the gradient of the deformation gradient, we find

$$\langle \nu \nabla^2 \mathbf{A} | \mathcal{A}_\tau \rangle \approx D^{-1}_{mk} D^{-1}_{nk} \left\langle \nu \frac{\partial^2 \mathbf{A}}{\partial X_m \partial X_n} \middle| \mathcal{A}_\tau \right\rangle. \tag{18}$$

Similar to the conditional average of the Lagrangian pressure Hessian, the conditional average of the Lagrangian Hessian of $\mathbf{A}$ on the RHS can be reasonably assumed to be isotropic. As in [15], an isotropic linear damping model is used for the conditional average here. As the argument in [15] shows, the damping time scale is the integral time scale of the velocity field, denoted by T. Thus

$$\langle \nu \nabla^2 \mathbf{A} | \mathcal{A}_\tau \rangle \approx -D^{-1}_{mk} D^{-1}_{nk} \frac{\delta_{mn}}{3T} \mathbf{A} = -\frac{\mathrm{Tr}\mathbf{C}^{-1}}{3T} \mathbf{A} \tag{19}$$

With $\mathbf{C}^{-1}$ replaced by $\mathbf{C}^{-1}_\tau$ as we did previously, we obtain the model for the diffusion term:

$$\langle \nu \nabla^2 \mathbf{A} | \mathcal{A}_\tau \rangle = -\frac{\mathrm{Tr}\mathbf{C}^{-1}_\tau}{3T} \mathbf{A}. \tag{20}$$

More details can be found in [15].

The model equation for $\mathbf{A}$ is completed by adding a random forcing term. Qualitatively the forcing term accounts for the neglected effects, such as the contributions from neighboring fluid particles and the external forcing. Following [15], we use an isotropic tensorial white noise forcing term. Putting the above models into Eq. (9), we obtain the stochastic equation for $\mathbf{A}$:

$$\begin{aligned} d\mathbf{A} = \Bigg[& -\mathbf{A}^2 - 2\boldsymbol{\Omega} \times \mathbf{A} - \frac{\mathbf{C}^{-1}_\tau}{\mathrm{Tr}\mathbf{C}^{-1}_\tau} (2\boldsymbol{\Omega} \cdot \boldsymbol{\omega} - \mathrm{Tr}\mathbf{A}^2) \\ & - \frac{\mathrm{Tr}\mathbf{C}^{-1}_\tau}{3T} \mathbf{A} \Bigg] dt + \frac{a'}{T^{1/2}} d\mathbf{W}, \end{aligned} \tag{21}$$

where $\mathbf{W}$ is a tensorial Wiener process. $d\mathbf{W} = \sqrt{2dt}\boldsymbol{\zeta}$ where $\boldsymbol{\zeta}$ is an isotropic traceless random tensor such that $\langle \zeta_{ij} \rangle = 0$ and $\langle \zeta_{ij} \zeta_{kl} \rangle = 2\delta_{ik}\delta_{jl} - 1/2\delta_{ij}\delta_{kl} - 1/2\delta_{il}\delta_{jk}$ (see, e.g., [19, 25]). a' is the magnitude of the forcing and has the dimension of the velocity gradient. In this work, we set $a' = 1/T$. More details on how to generate $\boldsymbol{\zeta}$ are given in [20].

2.3. *Stochastic model for scalar gradient*

The only unclosed term in the equation for the scalar gradient $\mathbf{G}$ is the molecular diffusion term. A model for $\mathbf{G}$ has been proposed in [19], where the ideas of the CM model are applied to the equation of $\mathbf{G}$. Detailed analyses are presented in [19] to demonstrate that the model reproduces realistically a range of kinematic and geometrical statistics of the scalar gradient. We will use this model here to investigate the effects of rotation on the mixing of passive scalars. According to

[19], the model equation for $\mathbf{G}$ can be written as

$$d\mathbf{G} = -\left(\mathbf{A}^T\mathbf{G} + \frac{\mathrm{Tr}\mathbf{C}_\tau^{-1}}{3T_\theta}\mathbf{G}\right)dt + \left(\frac{1}{T_\theta}\right)^{1/2} d\mathbf{W}_G, \tag{22}$$

where T_θ is the integral time scale of the scalar field, and $\mathbf{W}_G$ is a vectorial Wiener process independent of $\mathbf{W}$. Readers are referred to [19] for more details (note that to simplify notation $\mathbf{W}_G$ defined here is $\sqrt{2}$ times the one in [19]).

2.4. *Effects of rotation on recent fluid deformation*

The approximation is made in last section that $\mathbf{A}(s) \approx \mathbf{A}(t)$ for $t - \tau \le s \le t$, so that $\mathbf{D}(t)$ can be approximated by $\mathbf{D}_\tau(t)$. The approximation can be refined, as we will show now. Through the comparison between the two approximations, we will gain understanding on the impact of the approximations.

Given the Taylor expansion of $\mathbf{A}(s)$:

$$\mathbf{A}(s) = \mathbf{A}(t) + (s-t)\frac{d\mathbf{A}(t)}{dt} + \cdots, \tag{23}$$

we see that $\mathbf{A}(s) \approx \mathbf{A}(t)$ is a zero-order approximation keeping only the first term in the expansion. A natural refinement is to approximate $\mathbf{A}(s)$ by a higher order truncation. We consider the first-order approximation, where two terms in the Taylor expansion are kept. To obtain a closed expression, $d\mathbf{A}/dt$ in this expansion is approximated by a restricted-Euler type model (see, e.g., [26]). Namely, we omit the diffusion term, and replace the pressure Hessian by its isotropic part:

$$\nabla\nabla p \approx (\nabla^2 p)\mathbf{I} = (2\boldsymbol{\Omega}\cdot\boldsymbol{\omega} - \mathrm{Tr}\mathbf{A}^2)\mathbf{I},$$

where $\mathbf{I}$ is the identity matrix. The model for $d\mathbf{A}/dt$ (to be used to evaluate $\boldsymbol{D}_\tau(t)$) becomes

$$\frac{d\mathbf{A}}{dt} \approx -\mathbf{A}^2 - 2\boldsymbol{\Omega}\times\mathbf{A} - \frac{1}{3}(2\boldsymbol{\Omega}\cdot\boldsymbol{\omega} - \mathrm{Tr}\mathbf{A}^2)\mathbf{I}. \tag{24}$$

Evaluating the integral of $\mathbf{A}(s)$ in the time-ordered matrix exponential, one obtains the following alternative model for the inverse of the Cauchy-Green tensor:

$$\mathbf{C}^{-1} \approx e^{-\tau\mathbf{B}^T}e^{-\tau\mathbf{B}} \equiv \mathbf{C}_B^{-1}, \tag{25}$$

where we have used $\mathbf{C}_B^{-1}$ to denote the approximation, and

$$\begin{aligned}\mathbf{B} =& \mathbf{A} + (\tau/2)\left[\mathbf{A}^2 + 2\boldsymbol{\Omega}\times\mathbf{A}\right.\\ &\left.-(\mathbf{I}/3)(\mathrm{Tr}\mathbf{A}^2 - 2\boldsymbol{\Omega}\cdot\boldsymbol{\omega})\right].\end{aligned} \tag{26}$$

With $\mathbf{C}_\tau$ in Eq. (21) replaced by $\mathbf{C}_B$, we obtain a refined stochastic model for $\mathbf{A}$. The refined model will be called the first order model to distinguish it from the original zero-order model.

Whilst the first order model retains only one extra term in the Taylor expansion, the Cauchy-Green tensor now depends explicitly on the rotation rate. In other words, the direct effects of rotation on fluid deformation are partially captured. This is a qualitative difference between the two models. We will compare a number

of results of the first-order model with those of the zero-order model. Interestingly, we find that the results are very similar despite the qualitative difference between the models. The observation suggests that the zero-order truncation is a robust approximation. The comparison is presented in the next section.

2.5. *Summary and Comments*

Eqs. (21) and (22) constitute a closed set of stochastic models for the velocity and the passive scalar gradients in rotating turbulence. We non-dimensionalize the equations using the integral time scale T. Using $*$ to denote the nondimensional quantities, we have $\mathbf{A}^* = \mathbf{A}T$, $\boldsymbol{\omega}^* = \boldsymbol{\omega}T$, $\tau^* = \tau/T$, $t^* = t/T$, $T_\theta^* = T_\theta/T$, $d\mathbf{W}^* = d\mathbf{W}/T^{1/2}$, and $d\mathbf{W}_G^* = d\mathbf{W}_G/T^{1/2}$. The dimensionless equation can be obtained with simple substitution. To simplify notations, we drop the asterisks so that the dimensionless model equation for the velocity gradient can be written as

$$d\mathbf{A} = \left[-\mathbf{A}^2 - \frac{1}{Ro}\mathbf{k}\times\mathbf{A} - \frac{\mathbf{C}_\tau^{-1}}{\mathrm{Tr}\mathbf{C}_\tau^{-1}}\left(\frac{\mathbf{k}\cdot\boldsymbol{\omega}}{Ro} - \mathrm{Tr}\mathbf{A}^2\right) - \frac{\mathrm{Tr}\mathbf{C}_\tau^{-1}}{3}\mathbf{A}\right]dt + d\mathbf{W}, \tag{27}$$

where $Ro \equiv 1/(2\Omega T)$ is the Rossby number. $\mathbf{k}$ is the unit vector in the direction of the rotation axis. The equation for the scalar gradient [Eq. 22] is formally unchanged as long as the variables are understood as dimensionless quantities. In particular, T_θ is understood as the ratio between the scalar integral time scale and the velocity integral time scale, and τ as the ratio between the Lagrangian decorrelation time and the integral velocity time scale.

We note that in the models the nonlinear production terms as well as the Coriolis force for the gradients are in closed forms. Thus they are particularly useful for exploring the effects of the interaction between the two dominant processes in rotating turbulence. Our model for the velocity gradient is a generalization of the CM model in [15]. A number of ideas in our derivation have been presented in [15], including the Eulerian-Lagrangian coordinates substitution, the recent fluid deformation assumption, and the isotropic assumption for Lagrangian Hessians. We generalize the analysis to rotating turbulence, and derive a first-order model which incorporates the effects of rotation on the fluid deformation. Besides, we show that the isotropic assumptions for the Lagrangian Hessian tensors should be understood in terms of their conditional averages given the recent history of the velocity gradient tensor.

3. Numerical results and discussion

The stochastic models are solved numerically using a second-order weak predictor-corrector scheme [15, 27]. The computation starts from Gaussian random initial condition, where the velocity gradient $\mathbf{A}$ is initialized with traceless, statistically isotropic tensors with Gaussian random numbers as entries. For each set of parameters, 10^5 trajectories spanning over 100 integral time scales are computed, with a step size $dt = 10^{-4}$ (of the integral time scale T). The solutions show that the trajectories eventually approach a statistically steady state after a few integral time scales. The statistics are accumulated in the stationary stage.

To examine the effects of rotation, a number of Rossby numbers are considered. In order to compare with the results in the literature, we use the microscale Rossby

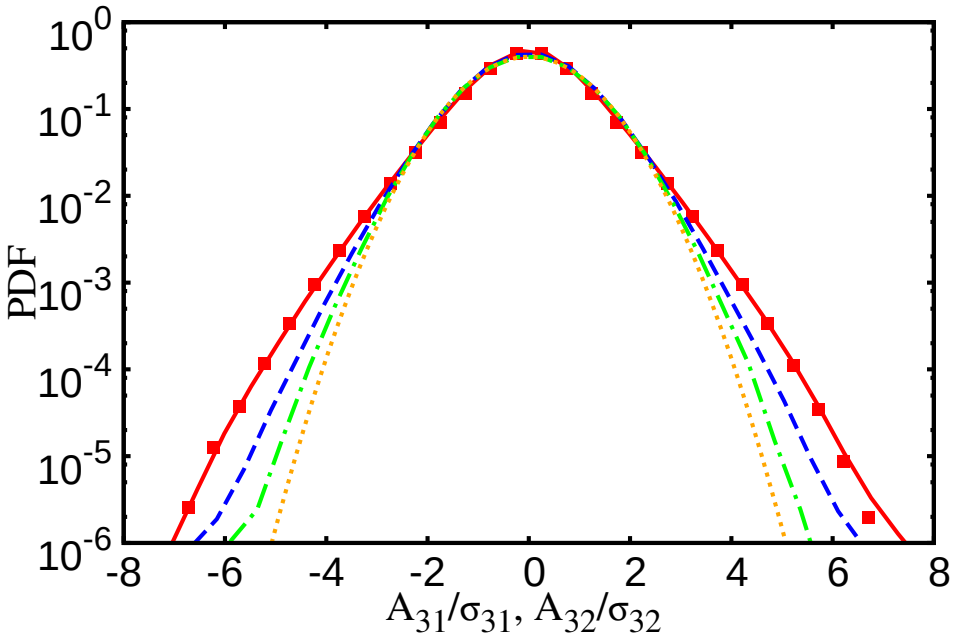

Figure 1. The PDFs of normalized normalized gradient A_{31}/σ_{31} and A_{32}/σ_{32}. Squares: without rotation; solid line: $Ro_\omega = 1.28$; dashed: $Ro_\omega = 0.2$; dash-dotted: $Ro_\omega = 0.01$; dotted: Gaussian distribution.

number $Ro_\omega \equiv \omega'/(2\Omega)$[6] , where ω' is the root mean square (RMS) value of the vorticity calculated from the numerical solutions. Ro_ω is a measure of the effects of rotation on small scales in turbulence. One expects that rotation has strong effects on small scales when Ro_ω is of order one or smaller. The values of Ro_ω in our calculation are 1.98, 1.28, 0.94, 0.59, 0.38, 0.26, 0.20, 0.09, 0.01. The corresponding rotation rates Ω are 0.67, 1.00, 1.33, 2.00, 2.86, 4.00, 5.00, 10.0, 100 in the unit of $1/T$. The results also depend on the two time scale ratios τ and T_θ. Note that the Lagrangian decorrelation time scale is of the order of the Kolmogorov time scale. Thus τ, as the ratio of the decorrelation time scale to the integral time scale, is related to the Reynolds number of the flow. We will present results for $\tau = 0.10$ only, corresponding approximately to $Re_\lambda \approx 150$ [20]. Simulations with $\tau = 0.08$ have also been conducted. Without showing the results, we only mention that the difference is small and is consistent with changes resulted from increasing the Reynolds number. T_θ is the scalar to turbulence integral time scale ratio. We use the value in [19], i.e. $T_\theta = 0.4$.

In what follows, the three coordinate directions are denoted by (x_1, x_2, x_3). The rotation axis is along the x_3-direction.

3.1. *Non-Gaussianity and anisotropy in the velocity gradient*

We first consider the effects of rotation on the non-Gaussian statistics in the velocity gradients. In homogeneous rotating turbulence, one expects the flow field to be axisymmetric, so that certain components of the velocity gradient have identical statistics. Our results show that the symmetry is maintained in the model. Therefore we have averaged some of the results over identically distributed components in what follows. The PDFs of the transverse gradients of the vertical velocity components A_{31} and A_{32} are shown in Figs. 1, for Rossby number $Ro_\omega = 1.28$, 0.2, and 0.01. The variables are normalized by their RMS values (denoted by σ). For comparison, the Gaussian distribution and the PDF without rotation (calculated from the models with $\Omega = 0$) are also plotted with dotted line and squares, respectively. Fig. 1 shows that, at $Ro_\omega = 1.28$, the PDFs of A_{31} and A_{32} are close to the ones

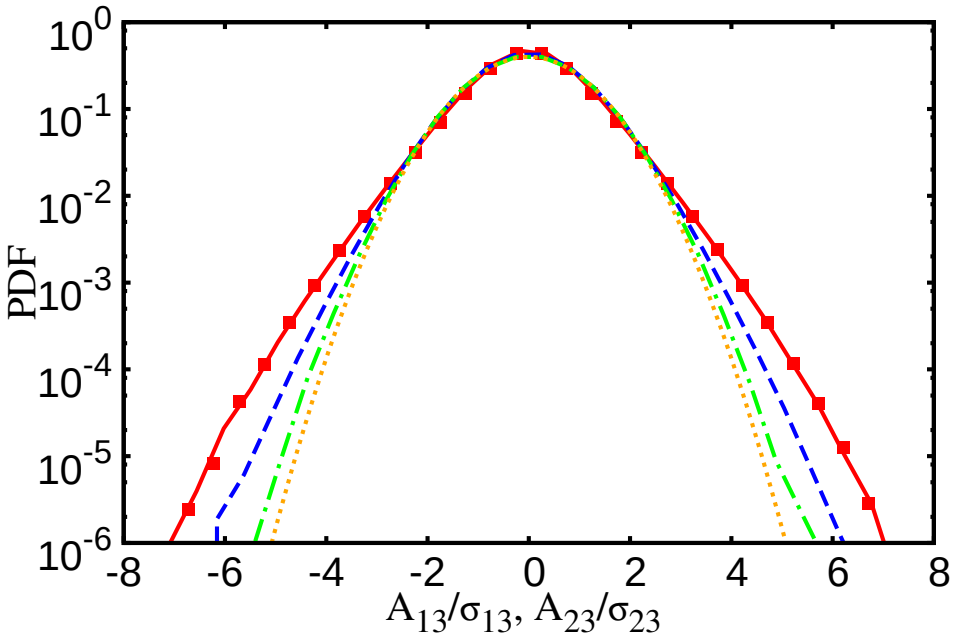

Figure 2. The PDFs of normalized gradient for A_{13}/σ_{13} and A_{23}/σ_{23}. Legend same as Fig. 1.

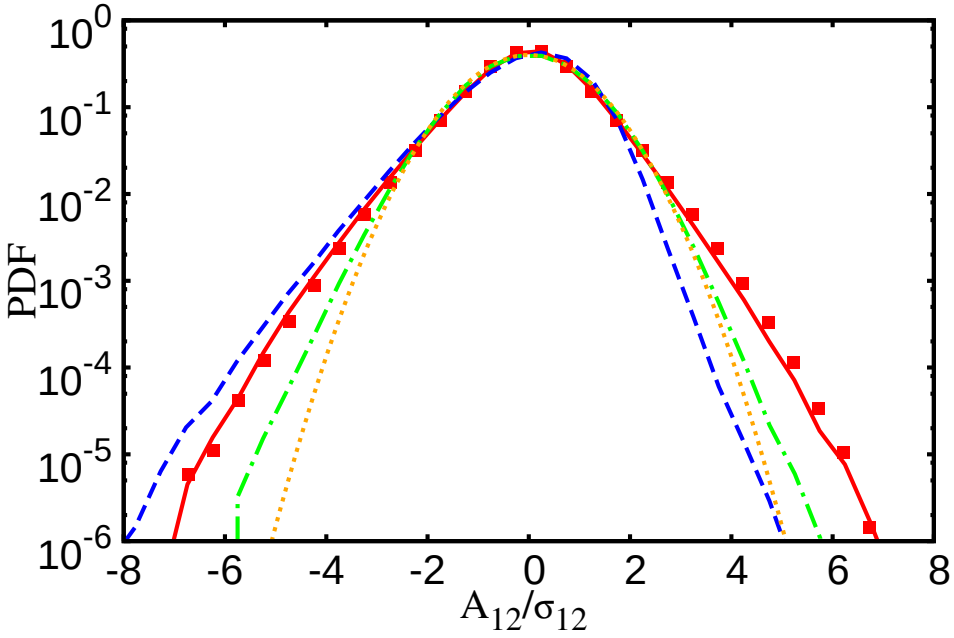

Figure 3. The PDFs of normalized A_{12}/σ_{12}. Legend the same as Fig. 1.

without rotation. The PDFs displays exponential-like tails, as is expected in non-rotating turbulence (see, e.g., [1]). When rotation rate is increased, the tails in the PDFs are suppressed, so that the probabilities for large fluctuations are reduced. The figure shows that the PDF tends to Gaussian distribution when the Rossby number tends to zero. Similar behaviors are observed in the results of A_{13} and A_{23}, the vertical gradients of the components perpendicular to the rotation axis. The PDFs of these two components are identical, and the average is plotted in Fig. 2. Figs. 1 and 2 show that the model reproduces the general effects of rotation on the intermittency of the velocity gradient.

Fig. 3 plots the PDFs of A_{12}. Similar to previous figures, at $Ro_\omega = 1.28$ the PDF

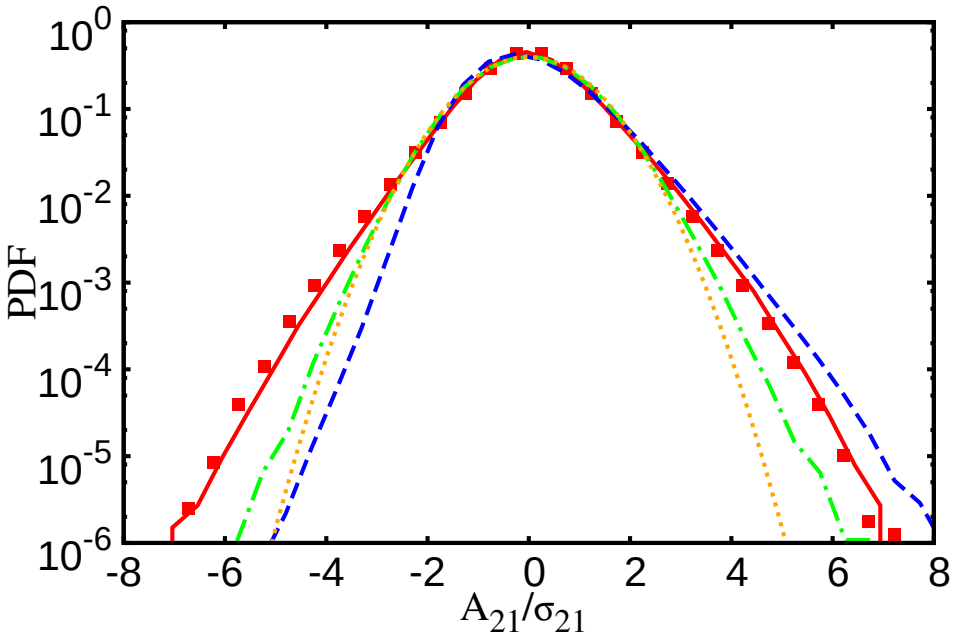

Figure 4. The PDFs of normalized A_{21}/σ_{21}. Legend the same as Fig. 1.

is not much different from the one without rotation, although slight asymmetry towards the negative direction can be seen. The PDF at $Ro_\omega = 0.2$, on the other hand, is strongly skewed towards negative fluctuations. The negative tail of the PDF is even 'fatter' than the one for zero rotation. Thus the probability to observe strong negative fluctuations is increased at this Rossby number. Meanwhile, positive fluctuations are suppressed. For further stronger rotation, on the other hand, the PDF tends to restore symmetry, and approaches the Gaussian distribution. This is illustrated by the dash-dotted line in the figure, which shows the PDF at $Ro_\omega = 0.01$. Since the skewness of A_{12} changes sign upon a reflection of the coordinate system with respect to a plane pivoted about the rotation axis x_3, non-zero skewness of A_{12} implies the lack of reflectional symmetry in the statistics. Asymmetric distribution is also observed for the PDFs of A_{21}, which are shown in Fig. 4. As is given by the dashed line, the PDF at $Ro_\omega = 0.2$ skews heavily towards the positive direction, in opposition to that of A_{12}. Due to the axisymmetry of the statistics, $-A_{12}$ and A_{21} have same statistics. This is the reason why A_{12} and A_{21} have opposite skewness. At $Ro_\omega = 0.01$, the PDF again appears to have restored symmetry and tends to Gaussian.

The skewness of $-A_{12}$ and A_{21} are plotted as functions of the Rossby number in Fig. 5. The skewness of a variable X is defined as $S(X) = \langle (X - \langle X \rangle)^3 \rangle / \langle (X - \langle X \rangle)^2 \rangle^{3/2}$. The two curves in Fig. 5 fall on each other as expected. The non-monotonic behavior is clearly displayed. The skewness is around 0.2 at $Ro_\omega = 1.2$, which increases when Ro_ω is decreased, and reaches the maximum value 0.64 at $Ro_\omega \approx 0.2$. It starts to decrease when the Rossby number is further decreased, and tends to zero when $Ro_\omega \to 0$. The curves show that the skewness has appeared even for rather weak rotation. (A number of data points calculated from the first-order model are also plotted in Fig. 5 with the squares. We will comment on that below. Similarly, in Figs. 6 and 7 we have also plotted results from the first-order model.)

No DNS result has been reported for the skewness of A_{12} and A_{21}. A related quantity is the skewness of the vorticity component in the direction of the rotation axis ω_3 (the cyclonic component). The latter has been measured in both DNS [5, 8, 28] and experiments [4]. The common observation is that ω_3 has positive

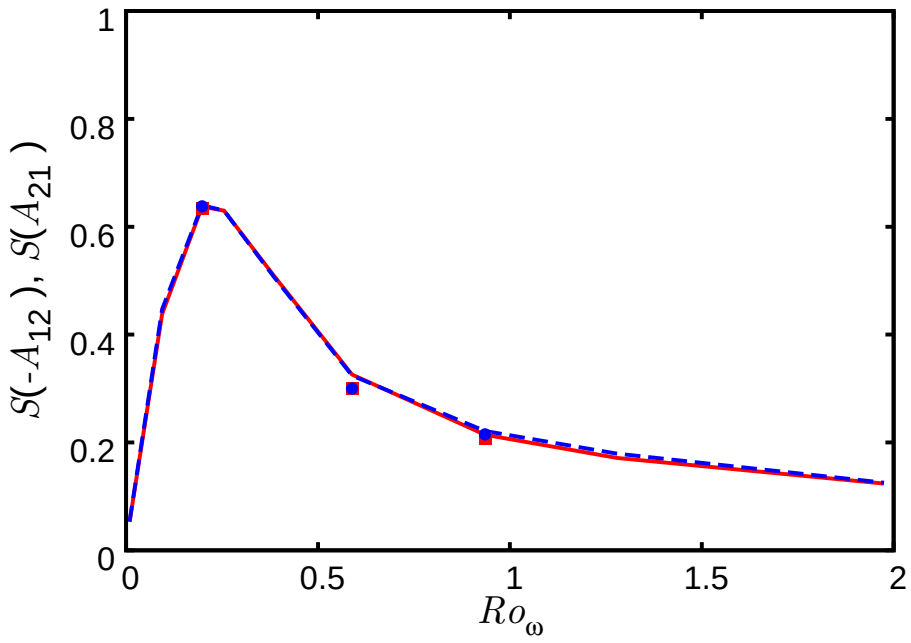

Figure 5. The skewness of A_{21} (solid line) and $-A_{12}$ (dashed) as the function of Rossby number. Symbols are calculated from the first order model.

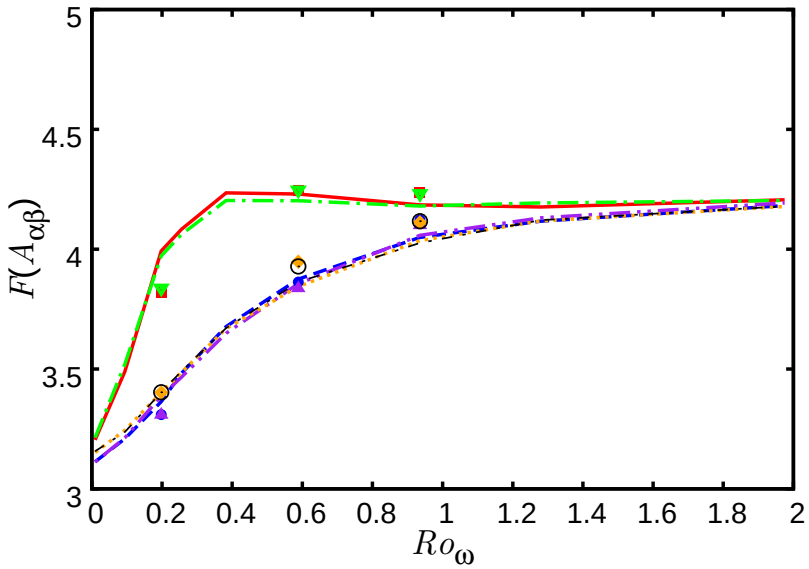

Figure 6. The flatness of the transverse velocity gradient components. The upper two curves are for A_{12} (solid line) and A_{21} (dash-dotted). The other four overlapping ones are for A_{13} (dashed), A_{23} (dash-dot-dotted), A_{31} (dotted), and A_{32} (thin dash-dotted). Symbols are the results calculated from the first order model.

skewness, and the skewness is the strongest for an intermediate Rossby number. In [8], the maximum is reached when $Ro_\omega = 0.2$, coincides with the value we obtained from the model. Since $\omega_3 = A_{21} - A_{12}$, when both A_{21} and $-A_{12}$ display positive skewness, one would expect that ω_3 have positive skewness as well. Unfortunately, the data of ω_3 calculated from the model (not shown) give no skewness for the Rossby numbers we have considered. The reason for the latter observation is not clear yet.

The reduction in the intermittency of the transverse velocity gradients can also be observed in their flatness. The flatness of a random variable X is defined as $F(X) = \langle (X - \langle X \rangle)^4 \rangle / \langle (X - \langle X \rangle)^2 \rangle^2$. Fig. 6 shows the flatness of all the transverse

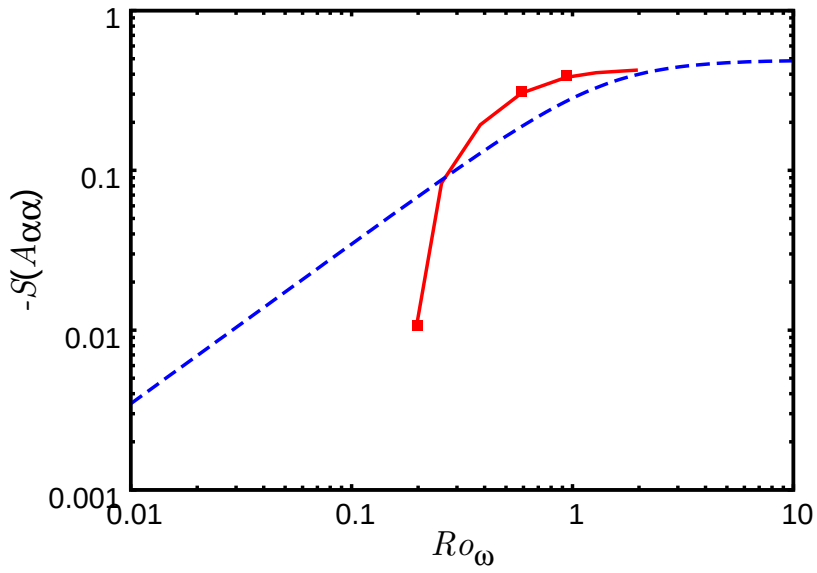

Figure 7. The skewness of the longitudinal velocity gradients as a function of Ro_ω calculated from the model (solid line). The dash line is the empirical expression $0.49/(1+2/(Ro_\omega)^2)^{1/2}$ (see text). The solid squares are calculated from the first order model.

components as functions of Ro_ω. The curves fall into two groups. Different curves in each group essentially overlap with each other. In the upper group are the curves for A_{12} and A_{21}, while in the lower group are the curves for the other components. For the components in the lower group, the flatness apparently is continuously reduced by rotation, and eventually approaches the Gaussian value 3 when the latter tends to zero. For A_{12} and A_{21}, the flatness stays nearly unchanged for Ro_ω down to approximately 0.35. From Fig. 3 (and Fig. 4) one can see that, even though fluctuations in A_{12} (A_{21}) with positive (negative) sign are suppressed by rotation for Rossby numbers in this range, large fluctuations with opposite sign are generated. Presumably, these fluctuations contribute to the flatness so that the latter keep a roughly constant value down to $Ro_\omega \approx 0.35$. When the Rossby number is further reduced, the flatness is also decreased and tends to the Gaussian value.

The model predictions on the skewness of the longitudinal velocity components are plotted in Fig. 7 with the solid line. An empirical expression for the skewness as a function of Ro_ω is proposed in [6], which provides a reasonably good fit to experimental and DNS results(see also [4]). The empirical expression reads

$$S(Ro_\omega) = \frac{-0.49}{(1+2/Ro_\omega^2)^{1/2}}, \tag{28}$$

and is also plotted in Fig. 7 with a dashed line for comparison. According to the formula, for large Ro_ω the skewness approaches -0.49 which is taken as the value in non-rotating turbulence. Fig. 7 shows that, for moderate Ro_ω values (say $Ro_\omega \geq 0.3$), model predictions are somewhat bigger than the values given by the formula. Nevertheless, the deviation is at the same order as the difference between the formula and experimental data (see, e.g., Fig. 7 of [4]). For smaller values of Ro_ω, the model results decrease too fast with Ro_ω. Thus, the model appears to over-predict the effects of rotation when it is strong, but it makes reasonable predictions on the skewness for moderate rotation.

Finally, we comment on the results of the first-order model. A number of data points calculated with the first-order model have been shown with symbols in Figs.

5, 6, and 7. While there are some small differences, the results are essentially the same as those obtained with the zero-order model. Similar behaviors are also observed in the results (not shown) for the PDFs. Therefore model results are not sensitive to the approximation where $\mathbf{A}(t)$ is assumed to be constant over its (short) recent history.

3.2. *Non-Gaussian statistics and local anisotropy of scalar gradient*

We now consider the effects of rotation on the non-Gaussian statistics of the scalar gradient. The model results for a passive scalar in non-rotating turbulence have been presented in [19]. For the purpose of comparison, some of the results will also be presented below.

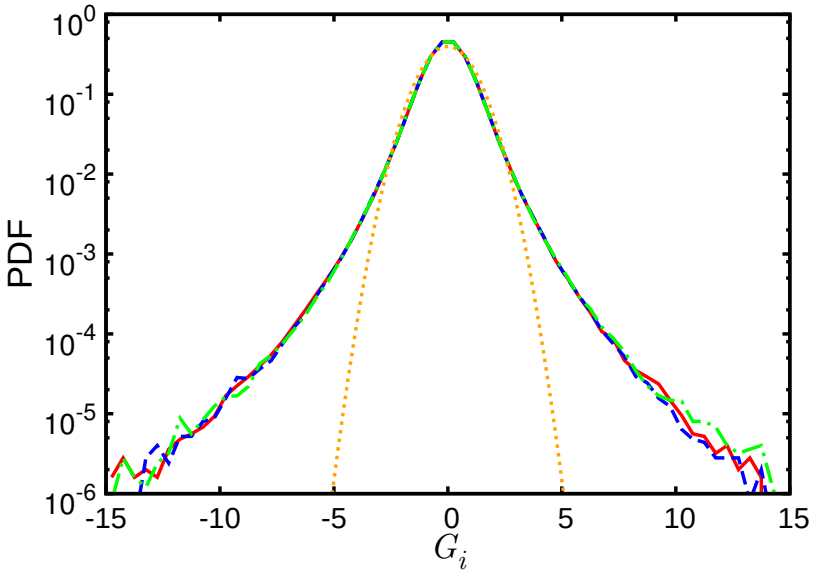

Figure 8. The PDFs of normalized passive scalar gradient calculated from the model without rotation. Solid line: G_1; dashed: G_2; dash-dotted: G_3; dotted: Gaussian distribution.

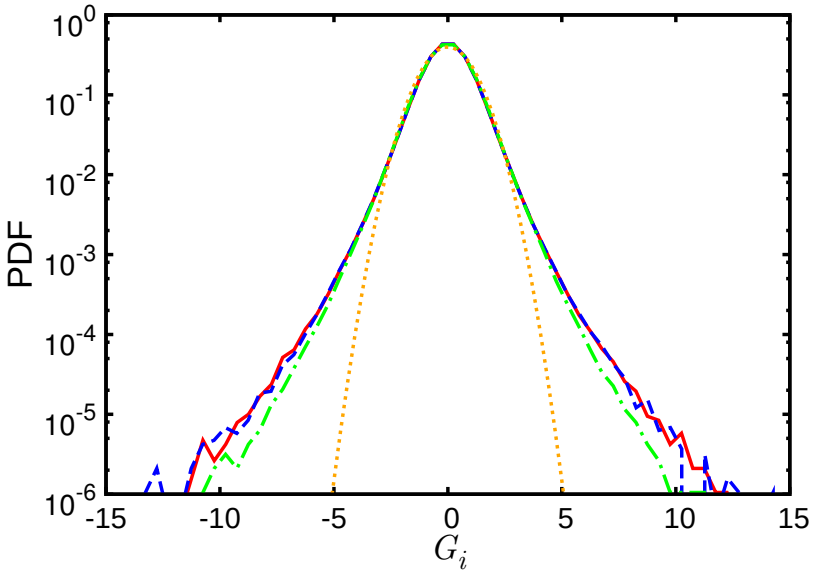

Figure 9. The PDFs of normalized passive scalar gradient. $Ro_\omega = 0.94$. Legend same as Fig. 8.

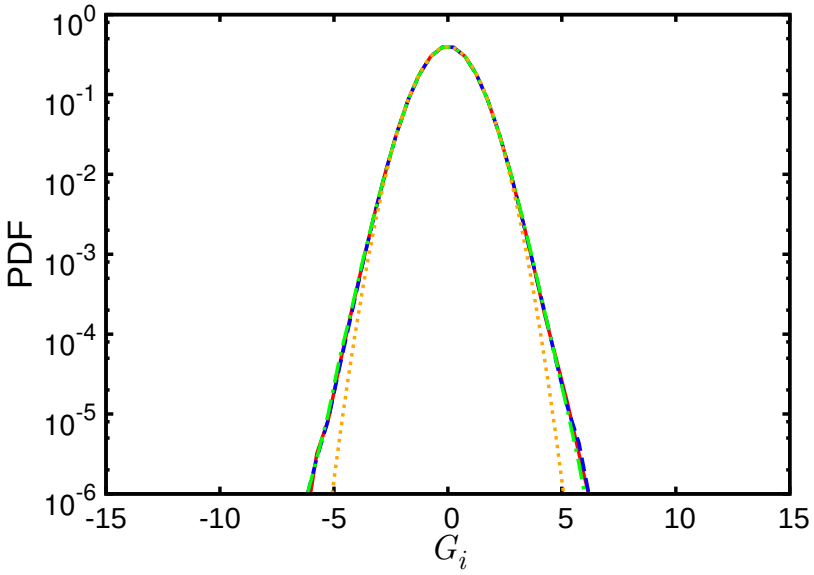

Figure 10. The PDFs of normalized passive scalar gradient. $Ro_\omega = 0.2$. Legend same as Fig. 8.

Ro_ω	∞	1.98	1.28	0.94	0.59	0.20	0.01
$F(G_\perp)$	8.50	7.33	6.32	5.95	4.48	3.24	3.03
$F(G_\parallel)$	8.49	6.49	5.42	4.82	4.04	3.28	3.00

Table 1. The flatness of the perpendicular and parallel components of the gradients of the passive scalar at different Rossby numbers.

Without rotation, the PDFs of the gradients of the passive scalar are plotted in Fig. 8. The PDFs display stretched exponential tails, as a consequence of small scale intermittency. The form of the PDFs is consistent with observations in turbulent flows, although the flatness is somewhat underestimated (see [19] and Table 1). Two observations can be made. First, the three components follow the same distribution. Second, comparing the PDFs with those of the velocity gradients (such as Fig. 1), we see that the scalar gradients are more intermittent. These observations reproduce the known results in isotropic turbulence. When rotation is imposed, the PDFs for $Ro_\omega = 0.94$ and 0.2 are given in Fig. 9 and 10, respectively. Comparing the figures, one can see generally rotation again tends to suppress large fluctuations. The PDFs tend to Gaussian distribution when rotation becomes increasingly strong.

Further observations can be made by a closer look at the PDFs at $Ro_\omega = 0.94$. Comparing the PDFs in Fig. 9, one can see that the PDF for G_3 decreases faster than the PDFs for G_1 and G_2. It implies that the gradient $\mathbf{G}$ is anisotropic at this Rossby number, and the component parallel to the rotation axis appears to be less intermittent than the other two components. The observation is consolidated with the data of the moments of the gradients. Our calculation shows that there is no significant difference in the RMS values of the gradients. Therefore, the anisotropy occurs mostly in large fluctuations, which can be characterized by flatness or higher order moments. For the flatness, we calculate the components perpendicular and parallel to the rotation axis separately, denoted by $F(G_\perp)$ and $F(G_\parallel)$, respectively. Without rotation ($Ro = \infty$), $F(G_\perp)$ is the same as $F(G_\parallel)$ (see Table 1) as a consequence of isotropy. When rotation is imposed, the results are plotted in Fig. 11 as well as given in Table 1. One observes that the flatness for both components decreases with the Rossby number, and at the strong rotation limit both tend to the Gaussian value 3. This is expected given the PDFs in Figs. 8-10 . More

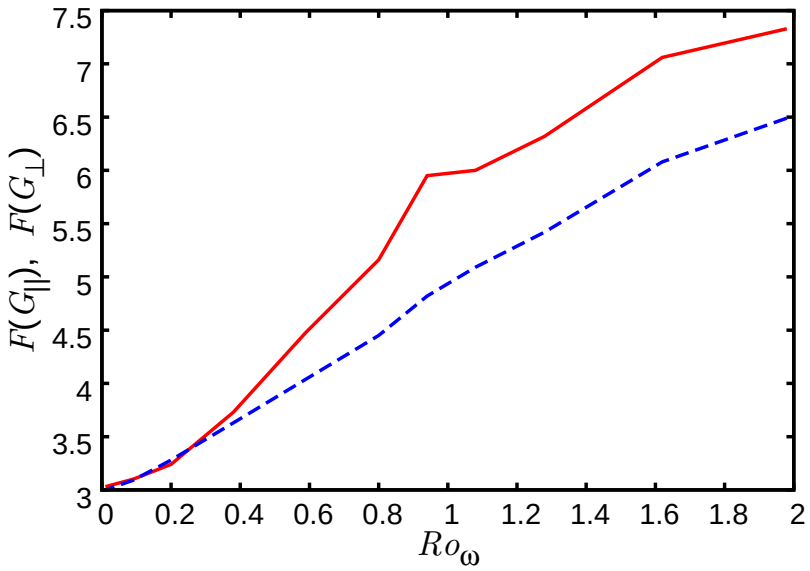

Figure 11. The flatness of the passive scalar gradient at different Rossby numbers. Solid line: the components perpendicular to the rotation axis ($F(G_\perp)$); dashed line: parallel component ($F(G_\parallel)$).

interestingly, the flatness of the perpendicular component $F(G_\perp)$ is significantly bigger than that of the parallel component $F(G_\parallel)$ for the whole range of Rossby numbers. Thus the observed local anisotropy in Fig. 9 is a generic behavior for the scalar gradient with rotation. Given that the difference between $F(G_\parallel)$ and $F(G_\perp)$ eventually disappears when either $Ro_\omega \to 0$ or $Ro_\omega \to \infty$, one can further infer that there must be an intermediate Rossby number for which the anisotropy is the maximum.

The anisotropy in the scalar gradient is also observed in a recent DNS study [9], where the mixing of a freely decaying scalar field in rotating turbulence is considered, and the flatness of the gradients at two Rossby numbers are presented. Thanks to the simplicity of the models, here we can obtain the dependence of the anisotropy on the Rossby number over a wide range of Rossby numbers. An explanation for the anisotropy is proposed in [9], where the anisotropy in $\mathbf{G}$ is believed to be due to the anisotropy in the spectral transfer functions for different components. The authors further argued that the anisotropy in the spectral transfer is due to large-scale anisotropy in the velocity field. In our model, however, there are no large scale fluctuations involved. Therefore, one may conjecture that there are also other mechanisms inherent to the dynamics of $\mathbf{G}$ and the velocity gradient $\mathbf{A}$.

To understand the possible mechanisms involved, we consider the transport equations for the marginal PDFs of the scalar gradient components G_α ($\alpha = 1, 2, 3$). Let $\mathcal{P}_\alpha(g_\alpha)$ denote the probability density for G_α being equal to a given value g_α. Using the model equation for $\mathbf{G}$ [Eq. 22], one can show that $\mathcal{P}_\alpha(g_\alpha)$ evolves according to the Fokker-Planck equation (for derivation see, e.g., [25]):

$$\frac{\partial \mathcal{P}_\alpha}{\partial t} + \frac{\partial}{\partial g_\alpha}\left[-\left\langle G_j A_{j\alpha} | G_\alpha = g_\alpha \right\rangle \mathcal{P}_\alpha\right] + \frac{\partial}{\partial g_\alpha}\left[-\frac{\left\langle \mathrm{Tr}\mathbf{C}_\tau^{-1} | G_\alpha = g_\alpha \right\rangle}{3T_\theta} g_\alpha \mathcal{P}_\alpha\right] = \frac{1}{2T_\theta}\frac{\partial^2 \mathcal{P}_\alpha}{\partial g_\alpha^2} \tag{29}$$

where repeated index α does not imply summation. Thus the stationary distribution is determined by the conditional averages of the production term (the second

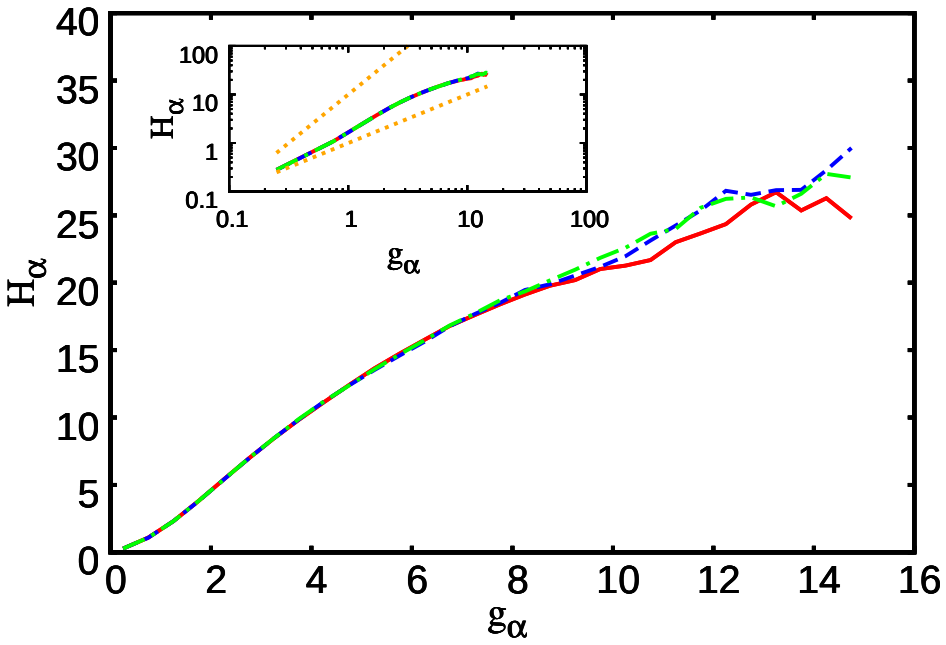

Figure 12. H_α as a function of g_α, without rotation. Solid line: $\alpha = 1$; dashed line: α_2; dash-dotted line: α_3. Inset: same results plotted in log-log scales. The two dotted lines have slopes 2 and 1, respectively.

term on the left hand side of the equation) and the damping term (the third term) in the model. Introducing the following notations for the various terms:

$$P_\alpha(g_\alpha) = -\langle G_j A_{j\alpha} | G_\alpha = g_\alpha \rangle \,,$$
$$D_\alpha(g_\alpha) = \frac{g_\alpha \left\langle \mathrm{Tr}\mathbf{C}_\tau^{-1} | G_\alpha = g_\alpha \right\rangle}{3T_\theta},$$
$$H_\alpha(g_\alpha) = -\int_0^{g_\alpha} [P_\alpha(s) - D_\alpha(s)] ds \,,$$

the stationary PDF is given by

$$\mathcal{P}_\alpha(g_\alpha) = C \exp[-2T_\theta H_\alpha(g_\alpha)], \tag{30}$$

where C is a normalization constant. The shape of the PDF is determined by H_α. For Gaussian distribution $H_\alpha(g_\alpha) \sim g_\alpha^2$, whereas $H_\alpha(g_\alpha) \sim g_\alpha$ for an exponential distribution. More generally, larger H_α implies the PDF has steeper slopes. H_α contains the competing effects of the production term P_α and the damping term D_α. The anisotropy observed in the PDFs is related to the anisotropy in P_α and D_α.

Fig. 12 plots H_α as a function of g_α when rotation is absent, for the three components $\alpha = 1, 2, 3$, respectively. As expected the three curves overlap with each other except for large g_α (say $g_\alpha > 9$), where statistical errors cause some discrepancy. The inset shows the same results in log-log scale. The curves at large g_α increase at a rate slower than linear. Therefore the PDFs have stretched exponential tails, as observed previously.

Fig. 13 shows the same results as Fig. 12 at $Ro_\omega = 0.94$. Even though some statistical errors are observed at large g_α, it is clear that H_3 is significantly bigger than H_1 and H_2. Given that $\mathcal{P}_\alpha(g_\alpha) \sim \exp(-2T_\theta H_\alpha)$, it means that the PDF $\mathcal{P}_3(g_3)$ decreases with its argument faster than $\mathcal{P}_2$ and $\mathcal{P}_1$. Thus the results for H_α are consistent with the PDFs. H_3 appears to increase linearly with g_3 for large g_3,

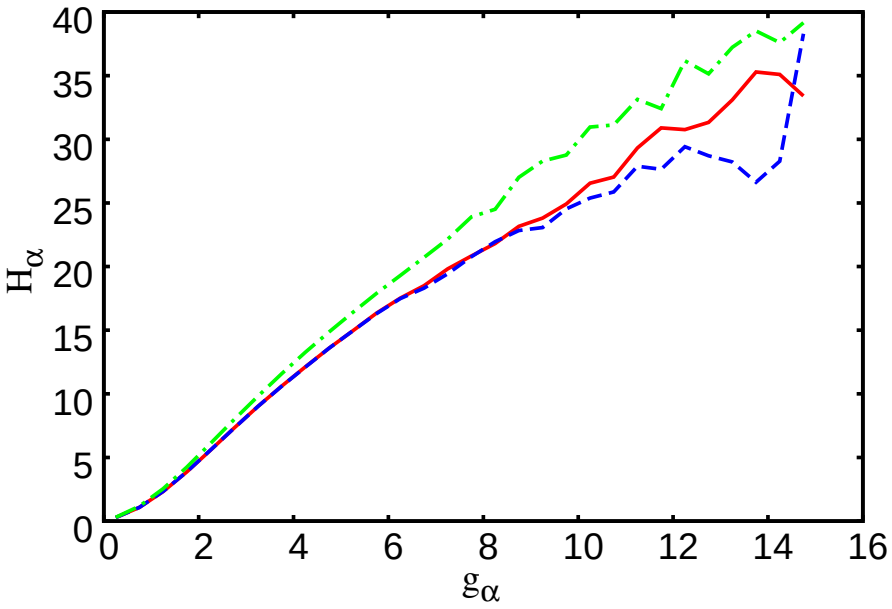

Figure 13. H_α as a function of g_α. $Ro_\omega = 0.94$. Legend same as Fig. 12.

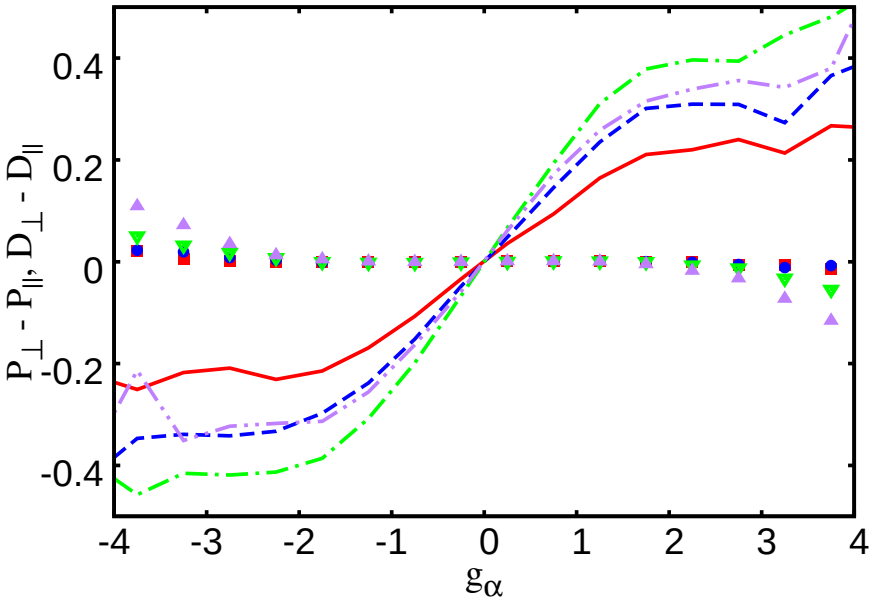

Figure 14. Lines: $P_\perp - P_\parallel$; symbols: $D_\perp - D_\parallel$. Solid line and squares: $Ro_\omega = 1.28$, dashed line and circles: $Ro_\omega = 0.94$, dash-dotted line and gradients: $Ro_\omega = 0.59$, dash-dot-dotted line and triangles: $Ro_\omega = 0.2$.

suggesting that $\mathcal{P}_3$ have exponential tails.

The difference in H_α ($\alpha = 1, 2, 3$) comes from the conditional averaged production term and viscous damping term. We examine the difference between different components of these two terms. Given that the two perpendicular components are statistically identical, we plot $P_\perp - P_\parallel$ and $D_\perp - D_\parallel$ as functions of g_α, where $P_\perp$ and $D_\perp$ are the averages of P_1 and P_2, and D_1 and D_2, respectively. When rotation is absent, P_α and D_α are isotropic so that the differences are zero (result not shown). The results at four finite Rossby numbers are shown in Fig. 14. We first observe that the results for the viscous damping term (symbols) are close to zero, implying that the perpendicular and parallel components of the damping term are nearly the same. This suggests that it is the production term, rather than the damping

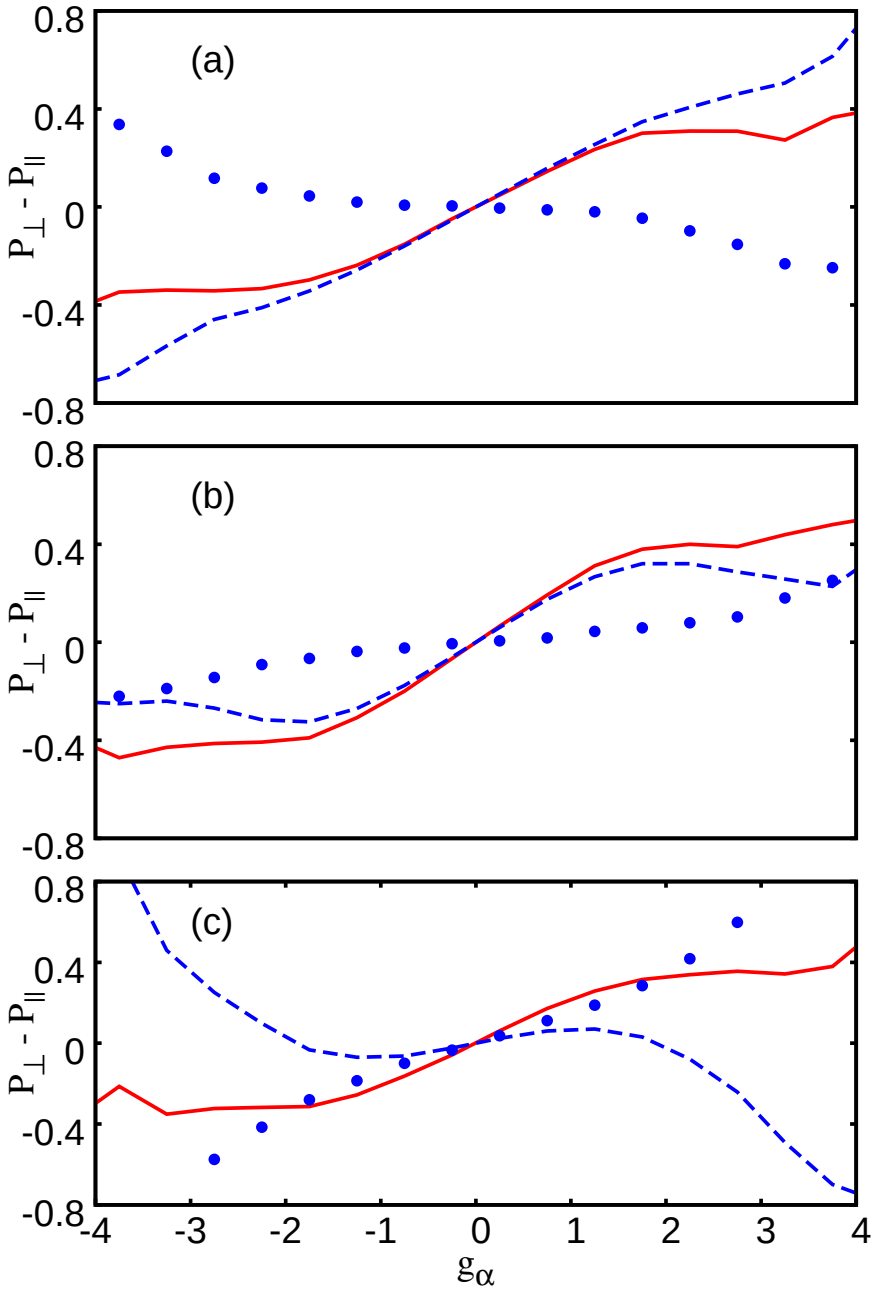

Figure 15. Solid line: $P_\perp - P_\parallel$; dashed line: contribution from the self-production term ; circles: contribution from cross-production terms. The sum of the latter two equals the former. Top: $Ro_\omega = 0.94$, middle: $Ro_\omega = 0.59$, bottom: $Ro_\omega = 0.20$.

term, that generates the anisotropy. Second, the difference in the production term (shown with lines), $P_\perp - P_\parallel$, increases when the Rossby number decreases from $Ro_\omega = 1.28$ through $Ro_\omega = 0.94$ to $Ro_\omega = 0.59$. However, the difference starts to decrease when Ro_ω is further reduced to 0.2. Therefore, the anisotropy appears to reach its maximum around $Ro_\omega = 0.59$, as far as the conditional averaged production term is concerned.

Note that, for each $\alpha = 1, 2, 3$, the production term P_α is the sum of three different terms: a self-production term $-\langle G_\alpha A_{\alpha\alpha} | g_\alpha \rangle$, and two cross-production terms. The self-production term generates scalar gradient by compressing iso-surfaces of the scalar together. The cross-production term, on the other hand, represents the production due to shearing and rolling-up of the iso-surfaces. Thus the difference in

$P_\perp - P_\parallel$ can be further decomposed into two contributions, one from the difference between the respective self-production terms in the perpendicular and the parallel components, and the other from the difference between the cross-production terms. Fig. 15 plots the two contributions for the three Rossby numbers around $Ro_\omega = 0.59$ where $P_\perp - P_\parallel$ is the maximum. The top panel shows that at $Ro_\omega = 0.94$, the self-production term (dashed line) makes positive contributions to the total difference $P_\perp - P_\parallel$ (solid line), whereas the cross-production terms (circles) make negative contributions. In other words, at this Rossby number the self-production terms for the perpendicular components dominate the one for the parallel component, whereas the cross-production terms for the latter dominates those for the former. On the other hand, when $Ro_\omega = 0.20$, the signs of the contributions are reversed (the bottom panel), i.e., the self-production term now makes negative contributions to the difference, whereas the cross-production terms make positive ones. Thus, there is a transition happening in the dynamics of the gradients. The figure in the middle panel shows that, during the transition at $Ro_\omega \approx 0.59$, the contributions from both self and cross production terms are positive. As a result, the difference in the whole production term $P_\perp - P_\parallel$ is the maximum.

The above analysis suggests that the anisotropy in the scalar gradients is related to the different responses of the self and cross production terms to rotation. The mechanisms should also exist in rotating turbulence regardless the large scale structures of the flow fields. It would be interesting to further the investigation with DNS analyses.

4. Conclusions

The properties of the velocity gradient and the gradient of a passive scalar in rotating turbulence are studied using Lagrangian stochastic models. The model for the velocity gradient generalizes a previous model [15] in which the recent fluid deformation history is used to construct closures for the pressure Hessian and viscous diffusion terms. We incorporate the effects of rotation into the closure for the pressure Hessian and the fluid deformation history. We show that the model assumptions should be formulated in terms of the conditional averages of the Lagrangian pressure Hessian and the Lagrangian viscous diffusion Hessian.

The model equations are solved numerically and the solutions are analyzed. The analyses focus on the effects of rotation on small-scale intermittency and local anisotropy of the gradients. It is found that the models reproduce the observations that rotation tends to weaken small-scale intermittency in both the velocity and the scalar gradients. For the velocity gradient, the model prediction on the skewness of the longitudinal components compares reasonably well with recent experimental data for moderate Rossby numbers. The models also predict the skewness of the perpendicular transverse components and its non-monotonic dependence on the rotation rates. For the scalar gradient, the models find the perpendicular components are more intermittent than the parallel component, as is observed in rotating turbulence. We show that the anisotropy increases initially but eventually disappear when the rotation becomes increasely stronger. The anisotropy measured by the conditionally averaged production term is the maximum at approximately $Ro_\omega = 0.59$, where a transition happens in the relative strength of the self-production terms and cross-production terms for different components.

We emphasize that the above results are obtained using stochastic Lagrangian models. Thus, further DNS and/or experimental studies are needed in order to draw definite conclusions. Besides, the quantitative agreement between the model predictions and DNS/experimental results need to be improved. For example, the

model over-predicts the effect of rotation on the skewness of the longitudinal velocity gradients when rotation is strong. Nevertheless, the analyses have shown that the qualitative aspects of the predictions are robust and do not depend on specific model assumptions. Further research can be pursued on several fronts. First, in rotating turbulence, it has also been observed that the Schmidt number has an effect on the level of anisotropy in the scalar gradient. However, the model for the scalar gradients implicitly assumes the Schmidt number being close to one, so has not included the effects of the Schmidt number. Second, as is mentioned in [15, 19], further investigation is needed for the models to make accurate predictions at high Reynold numbers. Finally, it would also be interesting to use DNS/experimental data to examine how rotation affects some of the model assumptions, such as the process of Lagrangian decorrelation. Such studies might explain the discrepancy observed at strong rotations, and will also provide valuable information generally on the Lagrangian dynamics of rotating turbulence.

Acknowledgements

The author is grateful to Laurent Chevillard, Charles Meneveau, Claude Cambon, and Koji Ohkitani for helpful disscusions. The valuable suggestions of the referees are also gratefully acknowledged.

References

[1] K. R. Sreenivasan and R. A. Antonia. The phenomenology of small-scale turbulence. *Annu. Rev. Fluid Mech.*, 29:435–472, 1997.
[2] U. Frisch. *Turbulence: the legacy of A. N. Kolmogorov*. Cambridge universtiy press, Cambridge, 1995.
[3] P. K. Yeung, J. Xu, and K. R. Sreenivasan. Scaling properties in rotating homogeneous turbulence. *Proceeding of FEDSM'03, 2003 4th ASME/JSME Joint Fluids Engineering Conference*, 2003.
[4] C. Morize, F. Moisy, and M. Rabaud. Decaying grid-generated turbulence in a rotating tank. *Phys. Fluids*, 17:095105, 2005.
[5] L. J. A. van Bokhoven, C. Cambon, L. Liechtenstein, F. S. Godeferd, and H. J. H. Clercx. Refined vorticity statistics of decaying rotating three-dimensional turbulence. *J. Turbulence*, 9, 2008.
[6] C. Cambon, N. N. Mansour, and F. S. Godeferd. Energy transfer in rotating turbulence. *J. Fluid Mech.*, 337:303–332, 1997.
[7] X. Yang and J. Andrzej Domaradzki. Large eddy simulations of decaying rotating turbulence. *Physics of Fluids*, 16(11):4088–4104, 2004.
[8] L. Bourouiba and P. Bartello. The intermediate rossby number range and two-dimensional-three-dimensional transfers in rotating decaying turbulence. *J. Fluid Mech.*, 587:139–161, 2007.
[9] P. K. Yeung and J. Xu. Effects of rotation on turbulent mixing: Nonpremixed passive scalars. *Phys. Fluids*, 16:93, 2004.
[10] S. B. Pope and W. K. Cheng. The stochastic flamelet model of turbulent premixed combustion. *Twenty-second Symposium (International) on Combustion*, pages 781–789, 1988.
[11] S. S. Girimaji and S. B. Pope. A diffusion model for velocity gradients in turbulence. *Phys. Fluids A*, 2:242–256, 1990.
[12] M. Chertkov, A. Pumir, and B. I. Shraiman. Lagrangian tetrad dynamics and the phenomenology of turbulence. *Phys. Fluids*, 11:2394–2410, 1999.
[13] E. Jeong and S. S. Girimaji. Velocity-gradient dynamics in turbulence: Effect of viscosity and forcing. *Theoret. Comput. Fluid Dyn.*, 16:421–432, 2003.
[14] J. Martin, C. Dopazo, and L. Valino. Joint statistics of the scalar gradient and the velocity gradient in turbulence using linear diffusion models. *Phys. Fluids*, 17:028101, 2005.
[15] L. Chevillard and C. Meneveau. Lagrangian dynamics and statistical geometric structure of turbulence. *Phys. Rev. Lett.*, 97:174501, 2006.
[16] R. E. Meyers and E. E. O'Brien. The joint pdf of a scalar and its gradient at a point in a turbulent fluid. *Combust. Sci. Technol.*, 26:123, 1981.
[17] R. O. Fox. The fokker-planck closure for turbulent molecular mixing: Passive scalars. *Phys. Fluids A*, 4:1230, 1992.
[18] V. Babenko and A. Stavrov. Modeling of the joint pdf of a scalar and its gradient in turbulent mixing. *Flow Turbulence Combust.*, 82:211–231, 2009.
[19] M. Gonzalez. Kinematic properties of passive scalar gradient predicted by a stochastic lagrangian model. *Phys. Fluids*, 21:055104, 2009.
[20] L. Chevillard, C. Meneveau, L. Biferale, and F. Toschi. Modeling the pressure hessian and viscous laplacian in turbulence: comparisons with dns and implications on velocity gradient dynamics. *Phys. Fluids*, 20:101504, 2008.

[21] L. Chevillard and C. Meneveau. Intermittency and universality in a lagrangian model of velocity gradients in three-dimensional turbulence. *C. R. Mécanique*, 335:187, 2007.
[22] S. B. Pope. Pdf methods for turbulent reactive flows. *Prog. Energy Combust. Sci.*, 11:119–192, 1985.
[23] J. A. Langford and R. D. Moser. Optimal LES formulations for isotropic turbulence. *J. Fluid Mech.*, 398:321, 1999.
[24] Y. Li, L. Chevillard, G. Eyink, and C. Meneveau. Matrix exponential-based closures for the turbulent subgrid-scale stress tensor. *Phys. Rev. E*, 79:016305, 2009.
[25] S. B. Pope. *Turbulent flows*. Cambridge University Press, Cambridge, 2000.
[26] B. J. Cantwell. Exact solution of a restricted Euler equation for the velocity gradient tensor. *Phys. Fluids A*, 4:782–793, 1992.
[27] P. E. Kloeden and E. Platen. *Numerical Solution of Stochastic Differential Equations*. Springer, Berlin, 1999.
[28] P. Bartello, O. Mètais, and M. Lesieur. Coherent structures in rotating three-dimensional turbulence. *J. Fluid Mech.*, 273:1–29, 1994.